processes

MDPI

Article

Fractal Characteristics of Multi-Scale Pore Structure of Coal Measure Shales in the Wuxiang Block, Qinshui Basin

Rui Wang [1] and Mengyu Zhao [2,*]

[1] School of Ocean Sciences, China University of Geosciences (Beijing), Beijing 100083, China; wangrui@cugb.edu.cn
[2] School of Resources and Environment, Henan Polytechnic University, Jiaozuo 454003, China
* Correspondence: myzhao@hpu.edu.cn

Abstract

Due to the diverse origins of shale reservoirs, the coal measure shales of the Wuxiang block, Qinshui Basin typically exhibit fractal pore structures, which significantly influence shale gas occurrence and migration. Clarifying the fractal nature of pore structures is significant for the efficient development and utilization of shale gas. In this study, mercury intrusion porosimetry and liquid nitrogen adsorption experiments were conducted to develop a method that integrates pore compressibility correction and nitrogen adsorption for pore structure characterization. On this basis, this study analyzed the fractal characteristics of coal measure shale pore structures across multiple scales. The results reveal that coal measure shale pores exhibit a three-stage fractal pattern, consisting of three regions with pore diameters >65 nm (seepage pores), 6–65 nm (transition pores), and <6 nm (micropores). Samples with fractal dimensions of seepage pores (D_a) exceeding 2.9 and transition pores (D_1) exceeding 2.5 tend to have larger specific surface areas and more complex pore structures; this is indicated by the increased surface roughness of large-scale pores, which hinders gas seepage. Samples with lower fractal dimension of micropores (D_2)—in the range of 2.2–2.8—exhibit higher micropore development, larger specific surface area, and simpler pore structures, as demonstrated by a greater number of micropores and a more uniform pore distribution, which promotes gas adsorption.

Keywords: coal measure shale; pore structure; fractal dimension; mercury intrusion porosimetry; liquid nitrogen adsorption method

check for updates

Academic Editors: Hexin Huang, Wenming Ji and Zhikai Liang

Received: 15 September 2025
Revised: 27 September 2025
Accepted: 30 September 2025
Published: 9 October 2025

Citation: Wang, R.; Zhao, M. Fractal Characteristics of Multi-Scale Pore Structure of Coal Measure Shales in the Wuxiang Block, Qinshui Basin. *Processes* **2025**, *13*, 3214. https://doi.org/10.3390/pr13103214

Copyright: © 2025 by the authors. Licensee MDPI, Basel, Switzerland. This article is an open access article distributed under the terms and conditions of the Creative Commons Attribution (CC BY) license (https://creativecommons.org/licenses/by/4.0/).

1. Introduction

The efficient development and use of unconventional natural gas in coal measures can help to mitigate the scarcity of conventional oil and gas supplies through supplementary clean energy provision, alleviate coal mine disaster risk, and optimize production economics. Simultaneously, it significantly contributes to greenhouse gas reduction and supports China's "dual carbon" strategic objectives [1–3]. Recent advancements in shale gas exploration and development in China have resulted in a continuous increase in production [4,5]. Numerous studies have demonstrated that shale gas reservoirs in China have complex origins and a wide variety of types. Their pore structures exhibit complex features, with significant differences in pore size distributions. Consequently, the extraction of coalbed methane resources from these reservoirs is challenging [6,7]. Shale reservoirs are rich in nano- and micro-scale pores and fractures, which intersect to form an intricate pore–fracture network with low porosity, low permeability, and heterogeneity [8–10]. These

features influence the shale gas's adsorption/desorption, diffusion, and seepage properties to varying degrees. Among them, the fine description and quantitative characterization of reservoir properties are limited by the qualitative evaluation of the complexity of the shale's pore structures, which is typically performed using traditional testing methods.

For natural reservoirs, many pore structure characterization methods and theoretical models have been proposed. There are three main ways to characterize the pore space. Image-based approaches, such as X-ray computed micro-tomography (micro-CT) [11], focused ion beams (FIBs), and scanning electron microscopy (SEM) [12,13], reconstruct the pore space by superimposing image information from core samples to create highly accurate models that approximate the actual pore structure. Conceptual models that use skeleton particles, including the capillary (bundle) model [14] and spherical particle model [15], can explain the physicochemical properties of porous media, such as their mechanics, specific surface area, and adsorption behavior. Statistical models employ mathematical and statistical methodologies to construct porous media by extracting structural parameters from limited test images or experimental data, including simulated annealing [16,17], process-based simulation methods [18,19], multiple-point geostatistics [20,21], and machine learning approaches [22,23]. When constructing statistical models, establishing a porous hyperelastic constitutive model helps to describe finite deformation behaviors in porous materials under arbitrary initial stress conditions [24]. However, image-based approaches are limited by measurement accuracy and cannot fully reflect the overall structural characteristics of reservoirs. In contrast, statistical models rely on understanding the geometric morphology, pore distribution, and scale variation patterns of pore structures. A key direction in this field is the construction of full-scale porous media models using statistical fractal models based on complexity assembly patterns of actual pore structures.

Numerous studies have shown that unconventional natural gas reservoirs, as porous media, exhibit fractal features in their pore structure. Fractal geometry theory effectively reveals the complex and heterogeneous nature of reservoir pore structures [25–27]. Previous studies have quantitatively analyzed the pore surface roughness, distribution heterogeneity, and structural complexity using the fractal dimension of porous media. A fractal dimension approaching 2 indicates a smoother pore surface and less complex pore structure [28–30]. Fractal geometry theory has been applied to the classification of reservoir pore structures [31–33], quantitative characterization of pore structures [34–36], and prediction of permeability [37,38]. Specifically, fractal models have been validated for equivalently characterizing complex pore structures in fractal porous media, including the particle-filled fractal (pore solid fractal, PSF) model [39], intermingled fractal unit (IFU) model [40], fractal capillary bundle model [41], pore network models (such as in fracture/pore/fracture fractal porous media) [27,42], and pore-throat-solid-network-connectivity fractal porous media (PTSNCF) model [43]. Nevertheless, the precise construction of fractal porous media fundamentally requires a comprehensive analysis of the pore structure's fractal characteristics. Clarifying the variation in pore size and its controlling factors in the multi-scale pore fractal distribution can significantly enhance the evaluation effectiveness of complex reservoirs.

To accurately evaluate shale gas reservoir characteristics, extensive studies have focused on developing fractal dimension calculation models for shale pore structures and their relationship with reservoir properties. Significant attention has been given to improving the applicability of these models for determining the fractal dimension. Using mercury intrusion porosimetry (MIP) and gas adsorption tests, the suitability of the Menger sponge [44], Frenkel–Halsey–Hill (FHH) [45], and pore volume-Specific surface area (V-S) models have been investigated in determining the fractal dimensions of three kinds of pores in shale gas reservoirs [46]. Therefore, the applicable fractal dimension calculation model varies with different pore structure testing methods. Table 1 summarizes and compares

the studies above. Future research should clarify the most appropriate model for each experimental method, considering reservoir lithology and physical properties.

Table 1. Pore structure characterization methods and models.

Classification	Methods/Models	Advantages	Limitations
Image-based approaches	Micro-CT FIB SEM	High-resolution images of coal rock surface can be obtained, providing direct visual insight on the actual pore structure.	Limited observation scales and small field of view, resulting in incomplete pore distribution information.
Conceptual models	Capillary (bundle) model Spherical particle model	Abstracts pore, pore throat, or fracture into capillary or spherical particles, which helps to explain the mechanism of diffusion and seepage, mechanics of porous media, etc.	The pore structure is usually simplified based on idealized geometric shapes, making it difficult to fully describe its complexity and changeability.
Statistical models	Simulated annealing Process-based simulation Multiple-point geostatistics Machine learning	Establish a porous media model using mathematical and statistical methods based on a small amount of slice images or test data, with low cost, high efficiency, and adaptability for different types of pore structures.	The simulation results depend on the accuracy of the initial model and constraint condition and involve a degree of randomness.
Fractal models	PSF model IFU model Fractal capillary bundle model Pore network models PTSNCF model	Capable of characterizing complexity and heterogeneity of fractal porous media under the guidance of statistical models.	The adaptability range of different fractal porous media model is limited.
	Menger sponge model FHH model V-S model	Calculation model of fractal dimension based on MIP and gas adsorption tests data, which is useful for the quantitative evaluation of fractal characteristics of pore structures.	It is not applicable for calculating the fractal dimension of full-scale pore structures.

The primary controlling factors of pore structure fractal characteristics in shales across different regions and types are diverse and exhibit certain differences. Recent studies have suggested that the fractal dimension of reservoir pore structures is significantly influenced by mineral components, source rock thermal maturity, organic matter abundance, and reservoir burial depth [47–49]. Fractal analysis can also help in comprehending the relationship between the fractal features of shale pore structures and their adsorption capability [50]. In addition, for deep shale, the latest research [51] clarified the key factors influencing its pore structure heterogeneity through TOC, XRD, and gas adsorption experiments, highlighting the significant impact of micropores on the development of irregular pore structures. Therefore, it is necessary to conduct targeted research on the variables affecting the complexity of shale pore structures.

The limited quantitative and evaluative studies on the complexity of coal measure shale pore structures in the Wuxiang block of Qinshui Basin restrict comprehensive evaluations of regional shale gas potential. A previous study investigated the applicability of MIP and the low-temperature nitrogen adsorption method in characterizing the pore structure of high-rank coal [52] and identified a suitable range of tiny pore sizes in high-rank coal for characterization. The study thus provided theoretical and practical approaches for finely characterizing these pore structures. Therefore, this study quantitatively characterizes the fractal features of multi-scale pore structures in coal measure shales from the Wuxiang block using MIP data (before and after matrix compression correction), low-temperature

nitrogen adsorption data, and appropriate fractal dimension calculation models. This study reveals the relationship between the complexity of coal measure shale pore structure and its physical properties, including porosity and specific surface area, and aims to enhance the understanding of multi-scale pore characteristics in the region's coal measure shales, providing a reference for evaluating shale gas occurrence and transport properties.

2. Samples and Methods

2.1. Sample Collection

The Qinshui Basin, situated within the North China Fault Block–Taihangshan Fault Block, is an intermontane faulted basin that formed through the differential uplift of faulted blocks following the Late Paleozoic coal-forming period in North China (Figure 1a). A large-scale synclinore structure with an NNE-SSW orientation makes up Qinshui Basin's main body [49]. The internal structural lines primarily extend in the NNE direction and are dominated by open short-axis folds and high-angle normal faults.

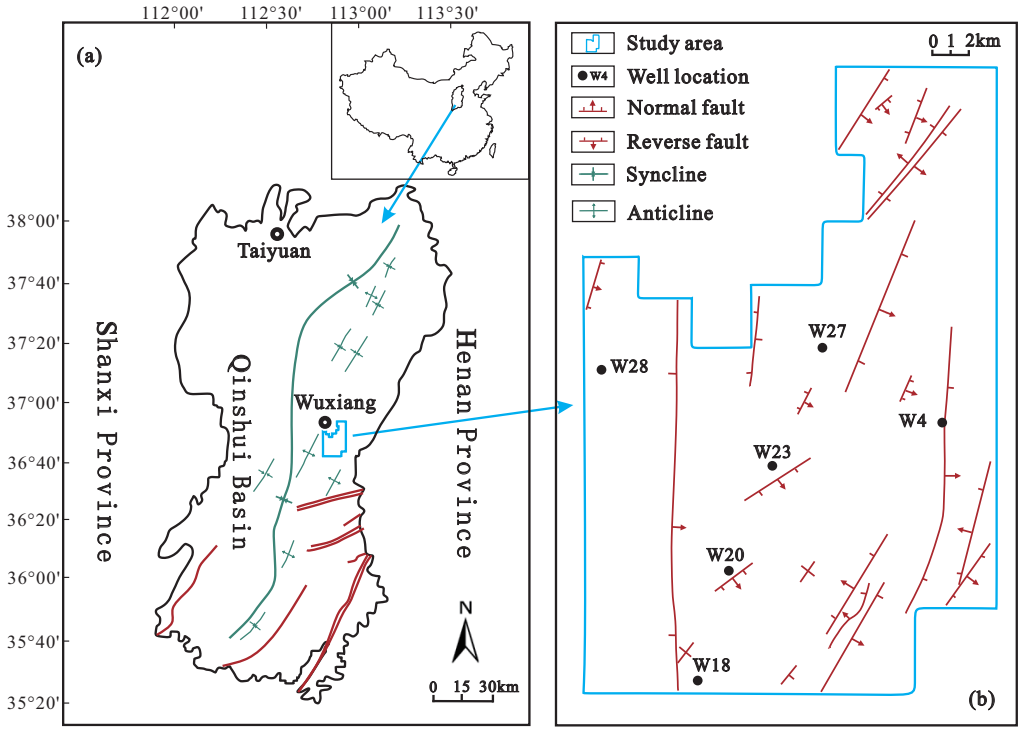


Figure 1. Tectonic map of the Wuxiang block in Qinshui Basin (modified from [49]). (**a**) Regional tectonic setting of Qinshui Basin, showing the location of Qinshui Basin, Wuxiang block, and the composite syncline structure. (**b**) Regional setting of the study area, showing the well locations of samples and the distribution of main and secondary faults.

The Wuxiang block, located in the eastern Qinshui Basin, serves as the study area. This region primarily comprises Paleozoic, Mesozoic, and Cenozoic strata and is rich in mineral resources, such as coal and aluminum, as well as animal and plant fossils [53]. The main coal seams in this region are located in the coal-bearing shale strata of the Taiyuan Formation (Upper Carboniferous–Lower Permian) and Shanxi Formation (Lower Permian) [54]. The thickness of the Shanxi Formation ranges from 36.83 m to 108.95 m, with an average thickness of 62.76 m. It comprises dark gray sandstone, mudstone, sandy mudstone, and coal seams, totaling four layers arranged from bottom to top as coal seam $4^{\#}$ through $1^{\#}$. The thickness of the Taiyuan Formation ranges from 102.85 to 184.15 meters. There are eleven coal seams in this formation, numbered $16^{\#}$ through $5^{\#}$ from bottom to top. The coal seams in the Taiyuan Formation primarily formed in a tidal flat depositional

environment with limestone–sand mudstone facies, and that in the Shanxi Formation formed in a deltaic interdistributary bay depositional environment, characterized by a mixed facies of mudstone, siltstone, peat, and black mudstone. More details of the coal seams can be found in [53].

Coal measure shale samples (W4-5, W18-6, W20-5, W23-1, W27-6, and W28-5) were collected from six gas wells in the Wuxiang block (Figure 1b), and their petrographic photos are shown in Figure 2. The specific depth of each sample is approximately 957 m($3^{\#}$), 1597 m($3^{\#}$), 1651 m($3^{\#}$), 1763 m($15^{\#}$), 1539 m($3^{\#}$), and 1902 m($15^{\#}$), respectively. The samples were primarily distributed in the top and bottom plates of the $3^{\#}$ and $15^{\#}$ coal seams. The $3^{\#}$ coal seam, located in the Shanxi Formation, is the primary coal seam within this formation, exhibiting stable occurrence with a thickness ranging from 0.38 m to 5.84 m. The $15^{\#}$ coal seam is located in the bottom clastic rock strata of the Taiyuan Formation, primarily composed of bioclastic micrite and sandy mudstone.

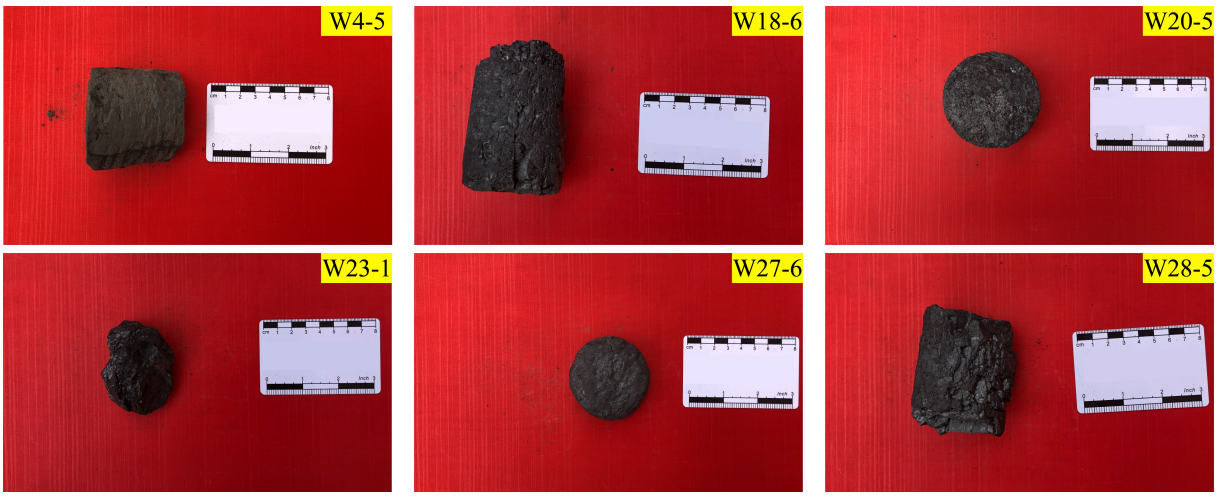


Figure 2. Photos of coal measure shale samples.

2.2. Testing and Processing Methods

We performed MIP and low-temperature nitrogen adsorption tests on the selected samples to investigate the pore structure characteristics of the reservoir in this region. MIP tests were conducted using the AutoPore9500 fully automatic mercury porosimeter, manufactured by Micromeritics Instrument Corporation (Norcross, GA, USA). It can measure pore diameter ranging from 5 nm to 1000 μm with a maximum pressure of 33,000 psi (228 MPa). Its key analytical capabilities include the measurement of pore size distribution, total pore volume, total pore area, bulk/true density, and fluid transport properties. An experiment was carried out following standard CB/T 21650.1-2008 [55]. Prior to MIP testing, the coal samples were crushed to achieve a uniform particle size of approximately 1 cm, dried at 110 °C for 24 h, and then placed in a desiccator to cool to room temperature. Then, a stepwise pressurization approach was adopted to test 99 pressure points, respectively, with a stabilization time of 10 s for each pressure point. According to the mercury injection pressure P_c, the pore diameter λ was deduced using the Washburn equation: $P_c(\lambda) = -4\gamma\cos\theta/\lambda$, where γ is the surface tension of mercury (N/m), and θ is the mercury contact angle with a solid surface (set to be 130°). The SA distribution was obtained using the Young–Dupré equation: yields $W_a = \gamma(1+\cos\theta)$, where W_a represents the work of adhesion between a liquid and a solid.

To compensate for the accuracy limitations of mercury intrusion porosimetry, we also conducted low-temperature nitrogen adsorption experiments. The automatic physical and chemical adsorption analyzer ASAP 2020 was chosen for specific surface area and pore size

analysis, manufactured by the Micromeritics Instrument Corporation (Norcross, GA, USA). Its measurement capabilities mainly include ultra-low surface area detection (0.0001 m^2/g), pore size analysis (1.7–300 nm), and modular upgrades (chemisorption, vapor adsorption). The experiment was conducted in accordance with standard SY/T 6154-1995 [56]. Prior to testing, six samples were crushed and ground to a particle size range of 0.3–0.45 mm. Then, they were dried in a vacuum oven at 80 °C for 24 h. Subsequently, they were purged with nitrogen and heated for degassing for 24 h to remove volatile substances on the pore wall surface. Afterwards, N_2 adsorption/desorption isotherms were measured at 77 K, and their relative pressure (p/p_0) ranged from 0.011 to 0.993. The specific surface area (SA), pore diameter, and pore volume (PV) of the samples were determined using BJH and BET methods.

2.3. Models for Calculating Fractal Dimensions of Pore Structures

Due to differences in fundamental principles, it is essential to use suitable models for calculating the fractal dimension of pore structures using different testing methods. Based on previous research results from different tests and their applicable fractal models [46,49], it is observed that the fractal dimension of macropores (>50 nm) is generally above 2.7, mesopores (2–50 nm), with an approximate range between 2.3 and 2.7. In addition, micropores (<2 nm) typically fall within a range of 2.0–2.2. These data were obtained through MIP and low-temperature nitrogen adsorption and carbon dioxide adsorption tests, respectively. Considering measurement accuracy, these findings suggest that higher precision measurements correspond to lower fractal dimensions.

However, the pore structure classifications in the aforementioned studies are primarily based on the IUPAC classification methodology. This approach relies on the physical adsorption of N_2 molecules in porous adsorbents, which has limitations when applied to coalbed methane reservoirs [57]. Consequently, to ensure measurement accuracy and result consistency, it is imperative to establish a precise classification of pore structures based on their fractal characteristics within the scale range of current tests.

(1) Mercury intrusion volume–pressure fractal model

Drawing inspiration from the construction of the Menger sponge model, a fractal model for determining fractal dimensions using mercury intrusion volume and pressure data from an MIP experiment was proposed [44], expressed as

$$\frac{\mathrm{d}V}{\mathrm{d}P_c} \propto {P_c}^{D-4}, \tag{1}$$

where $\mathrm{d}V/\mathrm{d}P_c$ corresponds to the relative change in mercury intrusion volume with pressure. The slope K is obtained by fitting the log–log plot of $\mathrm{d}V/\mathrm{d}P_c$ and P_c. The fractal dimension for pore structures with large-scale pore sizes can be determined using $D = 4 + K$. This model can be applied to calculate the pore volume fractal dimensions with a pore diameter greater than 50 nm.

(2) Adsorption volume–pressure fractal model

The fractal dimension of the pore volume from the gas adsorption experiment on fractal porous media is commonly calculated using the FHH fractal model [45], which is expressed as

$$\ln(V_{ad}) = K\left[\ln\left(\ln\left(\frac{p_0}{p}\right)\right)\right] + C, \tag{2}$$

where p represents the equilibrium pressure, V_{ad} denotes the pore volume or quantity adsorbed, p_0 represents the gas saturation pressure, and C serves as the constant term. For gas adsorption in fractal porous media, $K = D - 3$ during capillary condensation,

and $K = (D-3)/3$ when van der Waals interaction is involved. Based on previous studies [49,58], the applicable pore diameter range of the adsorption volume–pressure fractal model is approximately 2–100 nm.

2.4. Correction Method of MIP Experiments

Numerous studies have demonstrated that the high-pressure stage in mercury intrusion porosimetry experiments can deform matrix particles and pores in rock samples, resulting in a significant deviation between the pore volumes measured at high pressure and the actual situation [59–61].

Currently, the widely accepted correction method uses gas adsorption to obtain PV distribution data in the high-pressure range, and is then used to derive the matrix compression coefficient of shale [59], k_c:

$$k_c = \frac{dV_c}{V_c dP_c}, \tag{3}$$

where V_c represents the matrix volume, dP_c denotes the mercury intrusion pressure increment, and dV_c/dP_c reflects the change in matrix volume with pressure.

For compressible porous media, the variation in apparent mercury intrusion volume ΔV_{obs} is primarily influenced by coal matrix compression effects and pore-filling effects, satisfying

$$\Delta V_{obs} = \Delta V + \Delta V_c, \tag{4}$$

where ΔV represents the increment in actual pore volume or mercury intrusion volume after correction, and ΔV_c represents the compressive volume of the coal matrix. Combined with Equation (4), the value of dV_c/dP_c can be calculated as the difference between ΔV_{obs} and ΔV with the change in pressure, approximately satisfying

$$dV_c/dP_c \approx \Delta V_{obs}/\Delta P_c - \Delta V/\Delta P_c. \tag{5}$$

Previous studies [59,60] have demonstrated a strong linear relationship between mercury intrusion volume and pressure exceeding 10 MPa. Based on the observed deformation in the high-pressure stage and the linear relationship described by Equation (3), it can be inferred that this section represents the elastic deformation zone of matrix pores under high pressure. Therefore, the variation in mercury intrusion volume with pressure $\Delta V_{obs}/\Delta P_c$ in this range can be regarded as a constant C. The actual pore volume can be calculated using the N_2 adsorption test data with a pore diameter range from 5.5 to 120 nm. In substituting Equation (5) into Equation (3), the expression of k_c can be approximated as

$$k_c = \frac{1}{V_c}\left(C - \frac{\sum_{5.5nm}^{120nm} \Delta V}{\Delta P_c}\right). \tag{6}$$

In combining Equations (3) and (6) with the observed increment in mercury intrusion volume ΔV_{obs}, the corrected increment in mercury intrusion volume satisfies the relationship $\Delta V = \Delta V_{obs} - k_c V_c/\Delta P_c$.

3. Results and Discussion

3.1. Compressibility Correction of MIP Data

The pore volume distribution before and after the compressibility correction of MIP tests on the six samples is shown in Figure 3. The results in Figure 3a indicate a significant linear positive correlation between the cumulative mercury intrusion volume before correc-

tion and the mercury intrusion pressure of shale samples in the range of 10.32–227 MPa (corresponding to a pore diameter of 5.5–120 nm).

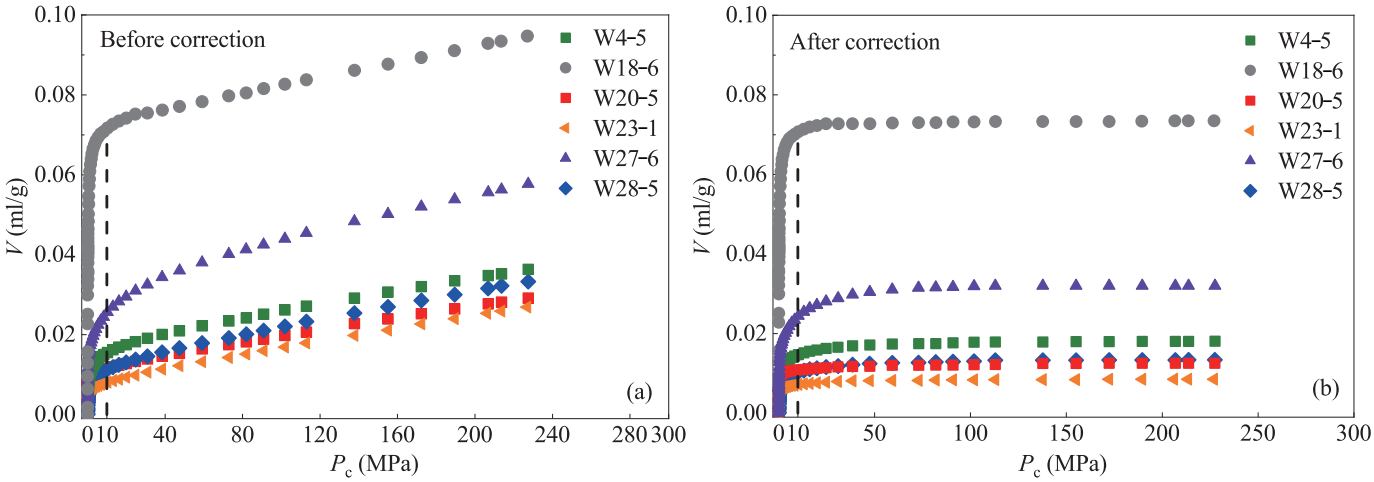


Figure 3. Plots of cumulative mercury intrusion volume for coal measure shale samples as a function of pressure (**a**) before and (**b**) after compressibility correction.

The results of the corrected MIP data are shown in Figure 3b. These findings indicate that the curve at the high-pressure stage reflects a linear increase before correction, while it transforms into a relatively stable horizontal line after correction. This fully verifies that the pore structures of the reservoir underwent elastic deformation during the high-pressure mercury intrusion stage.

Therefore, mercury intrusion volume data without compressibility correction were not applicable for extracting the fractal features of the pore structure. Meanwhile, the corrected matrix compressibility coefficients of the samples ranged between 1.121×10^{-10} and 1.968×10^{-10} $m^2 \cdot N^{-1}$ (Table 2), which is consistent with previous studies [62,63]. In addition, the results indicate that the k_c value of W27-6 is much higher than that of the other samples. Furthermore, the high adsorption volume may be attributed to the high transition pore and micropore content of the samples. Nevertheless, the combined effects of coal rank, coal lithotype, moisture content, microhardness, and tectonic deformation on k_c cannot be ruled out.

Table 2. Matrix compressibility and pore structure parameters of coal measure shale samples.

Sample ID			Mercury Intrusion Porosimetry		N_2 Adsorption
	ρ $(g \cdot cm^{-3})$	k_c $(10^{-10} \cdot m^2 \cdot N^{-1})$	V_b $(ml \cdot g^{-1})$	V_a $(ml \cdot g^{-1})$	V $(ml \cdot g^{-1})$
W4-5	1.533	1.252	0.02081	0.00336	0.00329
W18-6	1.378	1.352	0.01934	0.00266	0.00205
W20-5	1.504	1.121	0.01752	0.00166	0.00153
W23-1	1.505	1.282	0.01722	0.00132	0.00077
W27-6	1.654	1.968	0.03207	0.00759	0.00657
W28-5	1.415	1.312	0.02254	0.00297	0.00328

V_a and V_b, the mercury intrusion volume after and before correction, respectively; V, the adsorption volume.

However, it should be noted that the liquid nitrogen adsorption data for some samples did not fully include the 5.5–120 nm pore distribution information. Therefore, to ensure consistency, the mercury intrusion pressure range and the average pore size range must align with the selected liquid nitrogen adsorption data when calculating PV in this range.

3.2. Fractal Analysis of Pore Structures Using MIP Data

Based on MIP data, the distribution curves for mercury intrusion volume and pressure were plotted for coal measure shale samples both before and after correction, with the pore diameter ranging from 5.5 to 100,000 nm, according to Equation (1). In Figure 4, the value of dV/dP_c in Equation (1) was calculated as $\Delta V_{obs}/\Delta P_c$ and $\Delta V/\Delta P_c$, approximately, which reflects the change in mercury intrusion volume (before and after correction) with pressure.

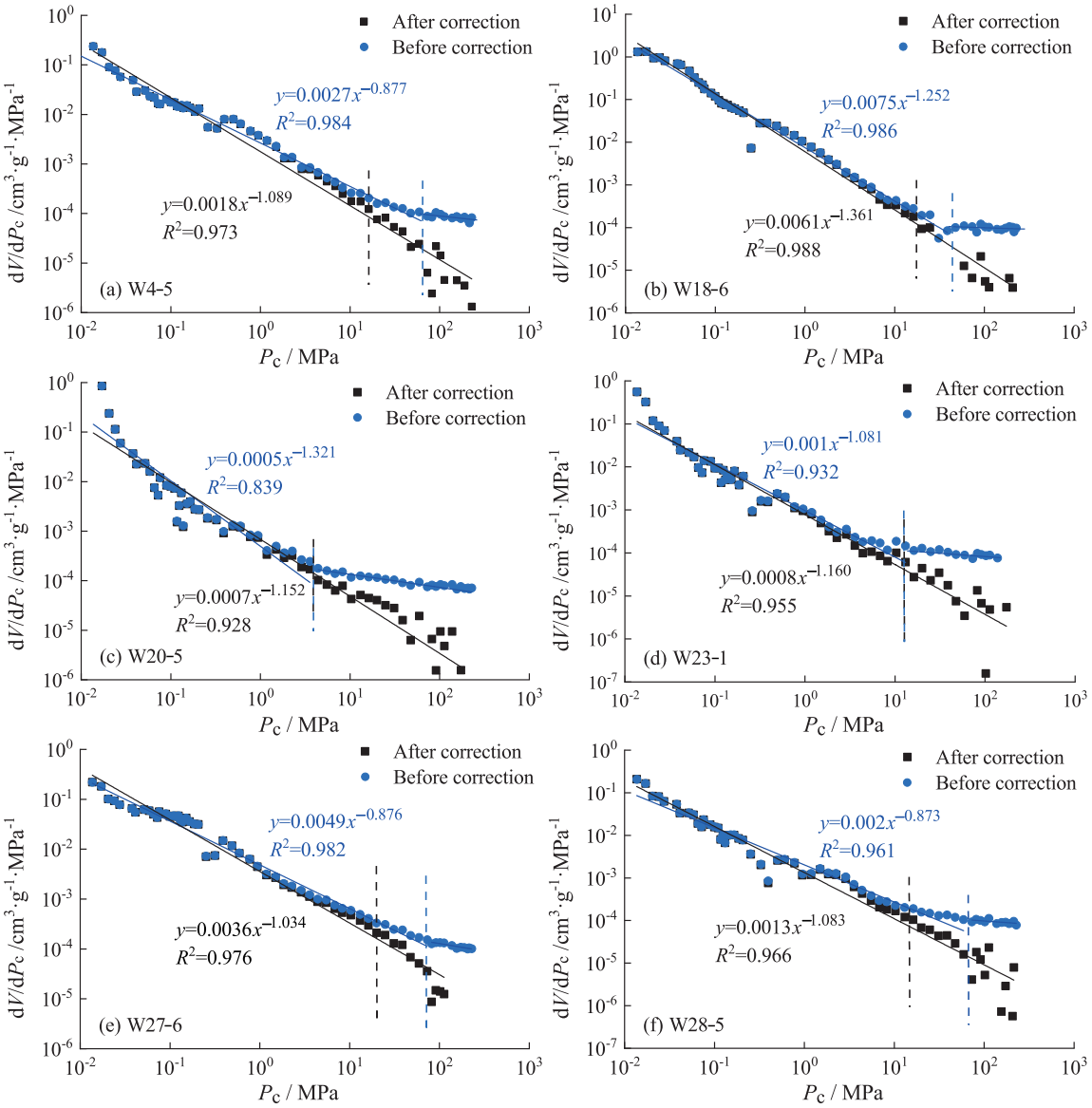


Figure 4. Log–log plots of dV/dP_c versus P_c for coal measure shale samples (**a**) W4-5, (**b**) W18-6, (**c**) W20-5, (**d**) W23-1, (**e**) W27-6, and (**f**) W28-5.

The results indicate the following: (i) The correlation of the corrected MIP data increased significantly within the entire pressure range. (ii) The correlation coefficient of the MIP data before and after correction was high within a low-pressure range, while notable differentiation within a high-pressure range (approximately > 10 Mpa). The log–log curves before correction of dV/dP_c versus P_c for all samples exhibit a stable trend in the high-pressure range, indicating coexisting pore structure characteristics across different scales. The corrected curves show significantly improved correlation, and the two types of structure characteristics are no longer evident. These results support the expectation of a uniform fractal pore structure background and highlight the difficulty in detecting

the micropore region under high pressure. (iii) The boundary between the two pore types before correction (blue dotted line) varies greatly, with pressures of 59.18 Mpa, 38.51 Mpa, 10.32 Mpa, 6.81 Mpa, 72.95 Mpa, and 59.18 Mpa, respectively. This inconsistency highlights the limitation of relying solely on the difference in pore fractal characteristics before correction to define the pore size ranges of the two pore types in shale samples. Through the comparison of the differences in log–log curves before and after correction, it was observed that most inflection points at which the mercury intrusion volume undergoes considerable changes before and after correction were approximately at a narrow space with a pore diameter ranging from 50 to 77 nm, except for sample W20-5. As shown in Figure 4c, the pressure of sample W20-5 at the inflection points is less than 10 MPa, whereas the pressures of other samples are above 10 MPa. The statistical result shows that the average value of the pore diameters corresponding to the inflection points of the five samples is approximately 67 nm.

In earlier studies, 65 nm is identified as the boundary for pore structure characteristics (seepage pore (>65 nm) and diffusion pore (<65 nm)) [31], based on their studies on the fractal classification of coal pore structure. This study used MIP testing data from 146 coal samples in China, including a subset of coal samples from this study area, which can partially address the issue of insufficient test samples in the present research. Utilizing this knowledge, we calculated the pore volume fractal dimensions at a pore diameter with >65 nm, <65 nm, and 5.5–10^5 nm before and after correction and list them in Table 3.

Table 3. Fractal dimensions of coal measure shale samples based on mercury intrusion data.

Sample ID	D_b			D_a		
	5.5–10^5 nm	**>65 nm**	**<65 nm**	**>65 nm**	**<65 nm**	**5.5–10^5 nm**
W4-5	3.204	3.105	3.7	3.062	2.396	2.911
W18-6	2.927	2.75	3.862	2.713	2.591	2.639
W20-5	3.346	3.077	3.818	2.769	2.667	2.848
W23-1	3.239	2.962	3.818	2.813	2.556	2.840
W27-6	3.178	3.098	3.504	3.063	2.118	2.966
W28-5	3.261	3.075	3.77	3.006	2.369	2.917

The results demonstrate the following: (1) The difference between the fractal dimensions of seepage pores before and after correction in the six samples was small. Additionally, the fractal dimension after correction D_a was generally smaller than that before correction D_b, indicating that the pore structure of this type of pores was affected by matrix compression to a certain extent. (2) The fractal dimensions of diffusion pores showed a significant difference before and after the correction of MIP data. Before correction, the fractal dimensions were all greater than 3, while less than 2.7 after correction, aligning more closely with reality. In summary, mercury intrusion porosimetry was only effective in characterizing the pore structure of seepage pores. Other methods must be used to characterize the pore structure of smaller pores.

3.3. Fractal Analysis of Pore Structures Using Liquid Nitrogen Data

The pore structure characteristics of diffusion pores (<65 nm) were determined by constructing log–log plots of adsorption volume versus relative pressure for each sample according to Equation (2), as shown in Figure 5. Except for samples W4-5 and W27-6, which exhibited minimal overall change, the slopes of the fractal curves for other samples show significant variation within the relative pressure p/p_0 ranging from 0.65 to 0.7 (approximately 6 nm). This indicates notable variations in the characteristics of pore structures. At a low range of $\ln(\ln(p_0/p))$, corresponding to a high relative pressure range

($0.65 < p/p_0 < 0.98$), the ln-ln plots of V_{ad} versus $\ln(p_0/p)$ for all samples show a good linear decreasing relationship. However, at a high range of $\ln(\ln(p_0/p))$, corresponding to a low relative pressure range ($0.2 < p/p_0 < 0.65$), there are distinct differences between the two groups of samples. The first group includes samples W4-5, W20-5, and W27-6, and the results show that there is a good decreasing relationship between $\ln(V_{ad})$ and $\ln(\ln(p_0/p))$, which is consistent with that at a low range of $\ln(\ln(p_0/p))$. In contrast, the results in the second group, including samples W18-6, W23-1, and W28-5, show a good increasing relationship. This indicates that the adsorption capacity of the pores in the low relative pressure range of the second group is significantly weaker than that of the pores in the high pressure stage, and even the adsorption capacity is less than the desorption capacity, resulting in a decrease in the adsorption capacity.

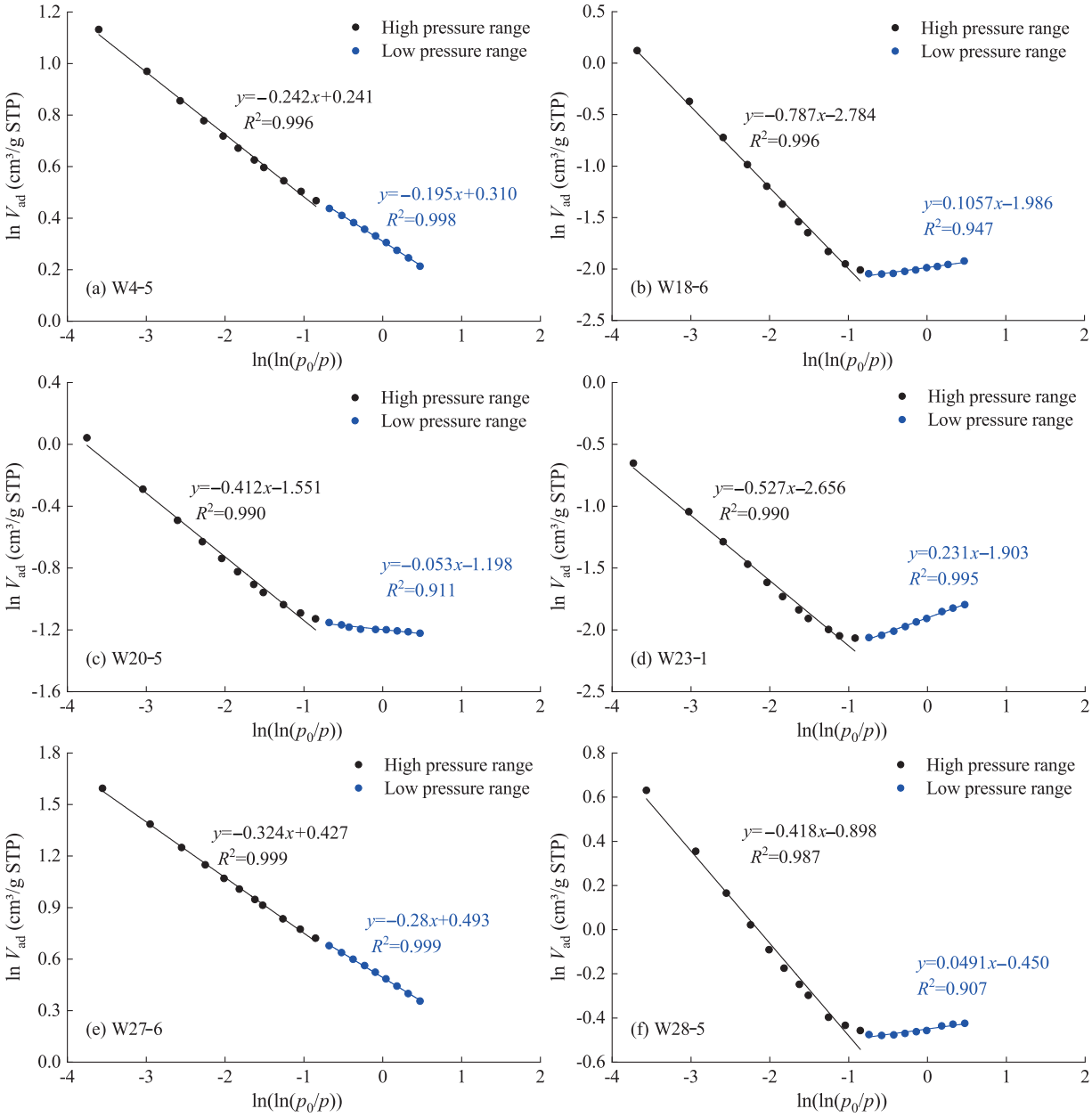


Figure 5. Ln–Ln plots of V_{ad} versus $\ln(p_0/p)$ for coal measure shale samples (**a**) W4-5, (**b**) W18-6, (**c**) W20-5, (**d**) W23-1, (**e**) W27-6, and (**f**) W28-5.

Based on a previous pore size classification of coal [57], the pore diameter range of transition pores varies greatly due to the differences in experimental types and analytical

methods, such as 10–100 nm, 15–50 nm, 1.2–30 nm, etc., which are generally in the range of 2–100 nm. Therefore, by referring to the current classification standard for the pore diameter range of transition pores, we further classified the diffusion pores of the coal measure shale in this region into transition pores (6–65 nm) and micropores (< 6 nm) based on the fractal characteristics of pore structures and the sudden change observed in the pore volume distribution curve. The PV fractal dimensions D_1 for each sample at the relative pressure p/p_0 ranging from 0.98 to 0.65 (6–65 nm) and the PV fractal dimension D_2 at $p/p_0 < 0.65$ (2–6 nm) are listed in Table 4.

Table 4. Fractal dimension of samples based on low-temperature liquid nitrogen adsorption data.

Sample ID	$D_1 = 3 + k$	R^2	$D_2 = 3 + 3k$	R^2
W4-5	2.758	0.996	2.414	0.998
W18-6	2.213	0.996	3.317	0.947
W20-5	2.588	0.990	2.841	0.911
W23-1	2.473	0.990	3.692	0.995
W27-6	2.676	0.999	2.159	0.999
W28-5	2.582	0.987	3.126	0.907

3.4. Relationship Between Fractal Characteristics of Pore Structure and Its Physical Properties

Based on the differences in pore structure fractal characteristics, the coal measure shales in this region have three different types of pores: seepage pores (>65 nm), transition pores (6–65 nm), and micropores (<6 nm). According to the corrected mercury intrusion porosimetry and nitrogen adsorption data, the PV and SA of each sample were obtained, as shown in Table 5. Among them, sample W18-6 failed to meet the minimum data integrity requirements for micropore analysis due to missing key parameters (such as BET surface area and pore volume) in its pore size distribution data . This was caused by technical issues during low-temperature liquid nitrogen adsorption testing, which prevented data acquisition for pore diameters below 6.3 nm. Therefore, it was not considered in the subsequent analysis.

Table 5. Measurements of the samples' pore volume and specific surface area for three pores.

Sanple ID	Seepage Pore		Transition Pore		Micropore	
	PV (cm^3/g)	SA (m^2/g)	PV (cm^3/g)	SA (m^2/g)	PV (cm^3/g)	SA (m^2/g)
W4-5	0.01557	0.14033	0.00268	0.57139	0.00102	1.38307
W18-6	0.07192	0.23443	0.00148	0.21660	/	/
W20-5	0.01115	0.05850	0.00116	0.19142	0.00003	0.05621
W23-1	0.00747	0.06528	0.00057	0.08914	0.00000	0.00008
W27-6	0.02637	0.25881	0.00510	1.09231	0.00157	2.01346
W28-5	0.01104	0.11664	0.00199	0.35385	0.00005	0.07845

For comparison, the PV and SA distributions of the seepage pores, transition pores, and micropores of each sample are normalized and displayed in Figure 6. In general, the PV proportion of transition pores in all samples is greater than that of micropores and smaller than that of seepage pores. However, significant differences are observed in the PV proportions across various pore types within each sample. This indicates that the PV of coal measure shale samples in this region was mainly controlled by the seepage pores. Conversely, the SA distribution data show that the proportion of SA of seepage pores in each sample is generally smaller than that of transition pores and micropores.

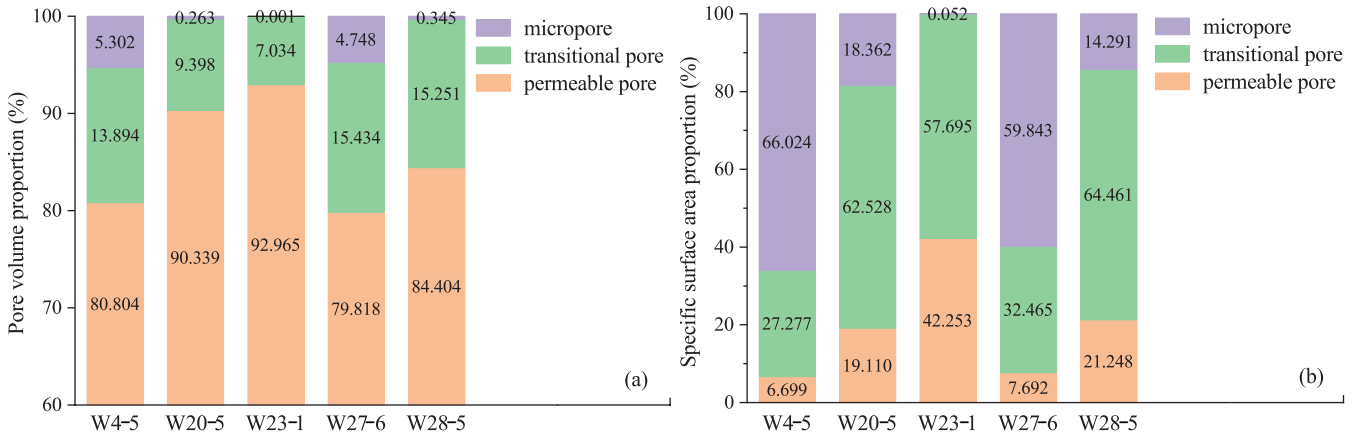


Figure 6. PV (**a**) and SA (**b**) proportions of three types of pores for coal measure shale samples.

To understand the effect of the fractal features of the pore structure on the porosity and SA of coal measure shale samples, the correlation between the PV and SA of pores at three pore scales is shown in Table 5. Moreover, their fractal dimensions are comparatively analyzed in Figures 7–10. The results demonstrated the following:

(1) The fractal dimensions of permeable and transition pores (D_a and D_1) in coal measure shale samples show a positive correlation with PV and SA, respectively, as shown in Figures 7 and 8. Among them, the correlations with SA in Figures 7b and 8b are relatively stronger than those with PV shown in Figures 7a and 8a. Specifically, when $D_a > 2.9$ and $D_1 > 2.5$, samples W27-6 and W4-5 show larger SA than the others, indicating that their pore structures are more complicated. When $D_a < 2.9$ and $D_1 < 2.5$, sample W23-1 shows a very low SA proportion. It is observed that there is a large fault and several secondary faults distributed near the locations of W27 and W4 (in Figure 1). This can lead to an uneven distribution of stress in the surrounding rock formations. The variability in the arrangement of internal joints and fractures increases, significantly enhancing the complexity of the pore structure. Therefore, the results in Figure 6 show groupings (W4-5 and W27-6) that may be affected by nearby faults. Furthermore, these results indicate that when the complexity of the pore structure reaches a high degree, its SA is likely to grow considerably. Combined with the PV proportion in Figure 6a, samples with smaller D_a exhibited higher relative development of seepage pores, whereas those with smaller D_1 showed lower relative development of transition pores. The higher agreement between the variations in D_a and the PV proportion of coal measure shale samples indicates that porosity was more significantly influenced by the fractal characteristics of seepage pores.

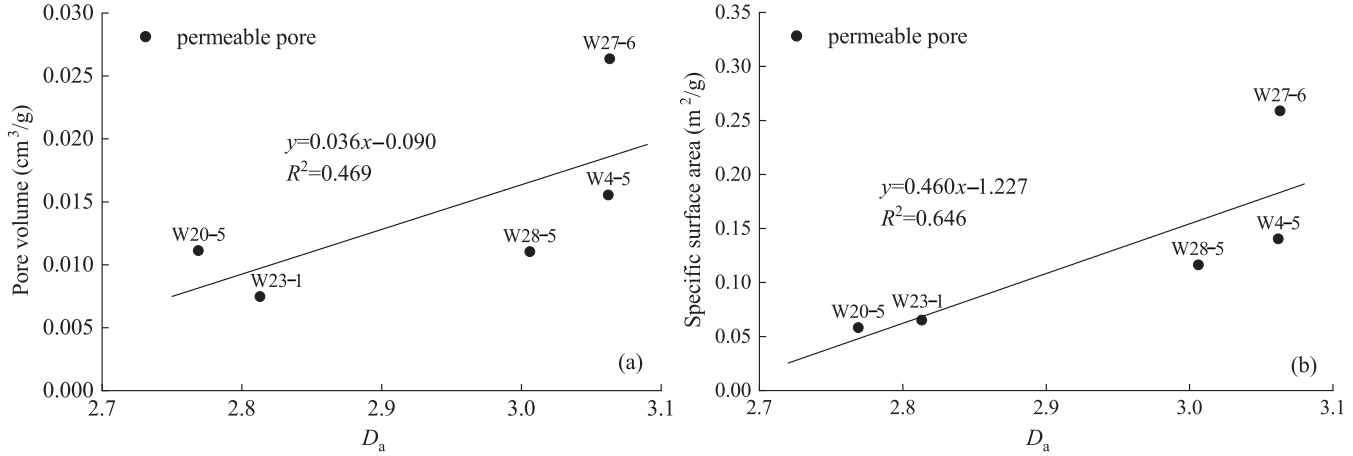


Figure 7. Relationships between pore volume (**a**) and specific surface area (**b**) with fractal dimensions of seepage pores.

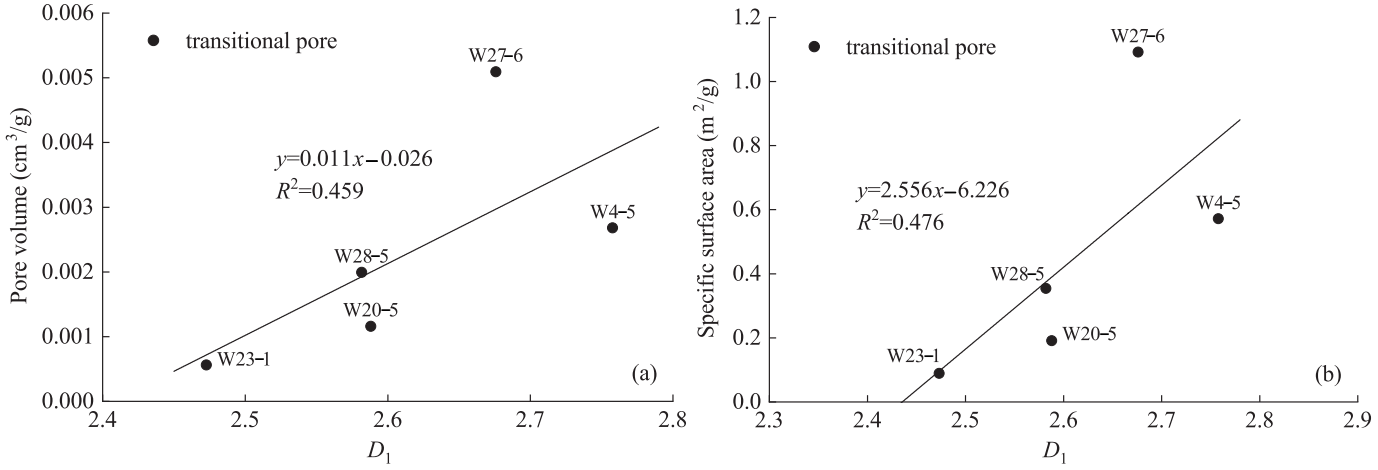


Figure 8. Relationships between pore volume (**a**) and specific surface area (**b**) with fractal dimensions of transition pores.

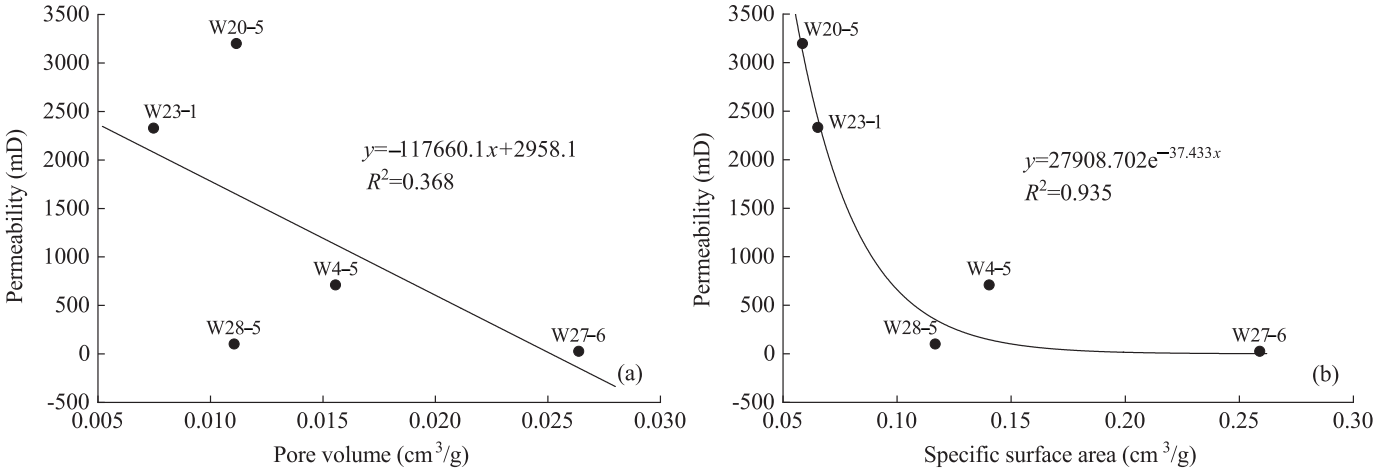


Figure 9. Relationships between pore volume (**a**) and specific surface area (**b**) with permeability of seepage pores.

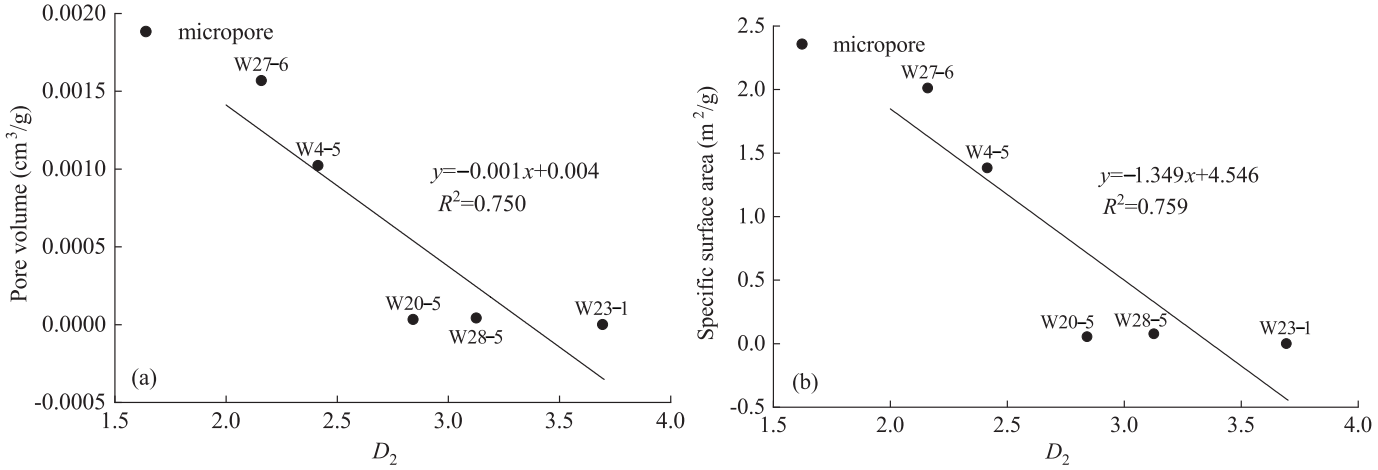


Figure 10. Relationships between pore volume (**a**) and specific surface area (**b**) with fractal dimensions of micropores.

To reveal the influence of PV and SA on gas seepage, the relationship curves between PV, SA, and the permeability of seepage pores were plotted using the permeability data directly obtained from MIP data, as shown in Figure 9. The results indicate that the SA

has a strong correlation with permeability, presenting a negative exponential relationship, while the correlation between pore volume and permeability is relatively weak. Combined with Figure 7b, higher fractal dimensions of seepage pores correlate with increased specific surface area, which leads to higher pore surface roughness and is less favorable for gas seepage.

(2) The PV and SA of micropores in coal measure shale samples negatively correlated with their fractal dimension D_2, as shown in Figure 10. The PV and SA are basically positively correlated with D_2 within the range of 2.2–2.8. This indicates that samples with smaller D_2 had a higher relative development of micropores and larger SAs, which is reflected as simpler pore structures, weaker heterogeneity of pore structures, and stronger gas adsorption capacity. Moreover, the trend lines of D_2 and SA (Figure 10b) exhibit the highest correlation among linear relationships in Figures 7, 8 and 10. This indicates that the effect of micropore fractal features on SA was more pronounced. Compared to D_1, D_2 had a higher correlation with PV and SA proportions, indicating that micropores significantly influenced the parameters of microscopic pore structure and related physical properties in the diffusion pores.

(3) Combined with the results in Tables 3 and 4, the fractal dimensions of seepage pores in Figure 7 ranged from 2.713 to 3.063 for all samples, those of transition pores in Figure 8 ranged from 2.213 to 2.758, and those of micropores in Figure 10 fluctuated significantly, ranging from 2.159 to 3.692. The maximum value of the difference between the fractal dimensions of seepage pores, transition pores, and micropores was 0.253 to 1.219. The minimum value was 0.072 to 0.5, and the average value of the fractal dimensions was generally above 2.7. This demonstrates that coal measure shales' pore structures in this region are highly complex, reflecting significant roughness and heterogeneity in their entirety.

This study focuses on the innovative exploration of fractal analysis methods to quantitatively describe the complexity of coal measure shale pore structure in the Wuxiang block. Beyond that, fractal analysis also has broader implications in shale gas exploration. The fractal dimension can be used to quantify the shale heterogeneity, guiding the design of hydraulic fracturing parameters (such as fracture spacing and fluid injection volume). Additionally, by integrating the characterization parameters of the fractal features of pore structures with production prediction models (such as fluid–structure interaction models and numerical simulation methods based on machine learning), the prediction accuracy of shale gas production can be enhanced to a certain extent. However, the systematic validation of fractal analysis in shale gas exploration and development applications requires the combination of more field data, advanced theory, and methodology. This will be a key focus of our work in the subsequent phase.

4. Conclusions

This contribution aimed to investigate the fractal characteristics of multi-scale pores in the region's coal measure shales and their influences on physical parameters. The following conclusions can be drawn:

(1) The fractal curves of mercury intrusion volume versus pressure before and after correction exhibited significant differences, enabling more accurate classification of pore structure types.The pore structures of coal measure shale samples show three distinct fractal characteristics across different scales. Consequently, the pore types of coal measure shales in this region were classified into seepage pores (>65 nm) and diffusion pores (≤65 nm). Diffusion pores were further subdivided into transition pores (6–65 nm) and micropores (<6 nm).

(2) The SA proportions of samples increase significantly as their D_a and D_1 reach high values ($D_a > 2.9$ and $D_a > 2.5$), reflected by a more complicated pore structure and higher surface roughness of large-scale pores. Samples with a lower D_2—namely, within the range of 2.2–2.8—have a comparatively higher degree of micropore development, a larger SA, and a simpler pore structure, indicated by a greater number of micropores and a more homogeneous pore distribution. The pore structure parameters of diffusion pores are more significantly influenced by micropores. The three types of fractal dimensions in each sample exhibited substantial variation, with an average value exceeding 2.7. This suggests that the overall pore structure of coal measure shale is extremely complex, characterized by a highly heterogeneous pore distribution and relatively high roughness.

Author Contributions: R.W. performed conceptualization, methodology, and funding acquisition; M.Z. performed writing—original draft. All authors have read and agreed to the published version of the manuscript.

Funding: This research was funded by Collaborative Education Project of the Ministry of Education with Industry (22053985265625), Open Fund of State Key Laboratory of Coal and Coalbed Methane Mining Technology in 2022 (2022KF13), National Natural Science Foundation of China (42402182), and the Fundamental Research Funds for Henan Polytechnic University (NSFRF2502114).

Data Availability Statement: Data will be made available on request.

Acknowledgments: We greatly appreciate the Editor and anonymous reviewers, whose valuable comments improved the manuscript.

Conflicts of Interest: The authors declare no conflicts of interest.

Abbreviations

The following abbreviations are used in this manuscript:

D_a	Fractal dimensions of seepage pores
D_1	Fractal dimensions of transition pores
D_2	Fractal dimensions of micropores
MIP	Mercury intrusion porosimetry
SA	Specific surface area
PV	Pore volume
micro-CT	Computed micro-tomography
FIB	Focused ion beams
SEM	Scanning electron microscopy
TOC	Total organic carbon
XRD	X-Ray diffraction
FHH	Frenkel–Halsey–Hill
V-S	Pore volume-Specific surface area

References

1. Li, L. Development of natural gas industry in China: Review and prospect. *Nat. Gas Ind. B* **2022**, *9*, 187–196. [CrossRef]
2. Liu, J.; Sun, H.; Lei, Y.; Cao, J. Current situation and development trend of coalbed methane development and utilization technology in coal mine area. *J. China Coal Soc.* **2020**, *45*, 258–267. (In Chinese)
3. Xu, F.; Hou, W.; Xiong, X.; Xu, B.; Wu, P.; Wang, H.; Feng, K.; Yun, J.; Li, S.; Zhang, L.; et al. The status and development strategy of coalbed methane industry in China. *Pet. Explor. Dev.* **2023**, *50*, 765–783. [CrossRef]
4. Zhao, J.; Ren, L.; Jiang, T.; Hu, D.; Wu, L.; Wu, J.; Yin, C.; Li, Y.; Hu, Y.; Lin, R.; et al. Ten years of gas shale fracturing in China: Review and prospect. *Nat. Gas Ind. B* **2022**, *9*, 158–175. [CrossRef]
5. Lei, Q.; Weng, D.; Guan, B.; Shi, J.; Cai, B.; He, C.; Sun, Q.; Huang, R. Shale oil and gas exploitation in China: Technical comparison with US and development suggestions. *Pet. Explor. Dev.* **2023**, *50*, 944–954. [CrossRef]

6. Chen, S.; Zhu, Y.; Wang, H.; Liu, H.; Wei, W.; Fang, J. Shale gas reservoir characterisation: A typical case in the southern Sichuan Basin of China. *Energy* **2011**, *36*, 6609–6616. [CrossRef]
7. Sun, C.; Nie, H.; Dang, W.; Chen, Q.; Zhang, G.; Li, W.; Lu, Z. Shale gas exploration and development in China: Current status, geological challenges, and future directions. *Energy Fuels* **2021**, *35*, 6359–6379. [CrossRef]
8. Josh, M.; Esteban, L.; Delle Piane, C.; Sarout, J.; Dewhurst, D.N.; Clennell, M.B. Laboratory characterisation of shale properties. *J. Petrol. Sci. Eng.* **2012**, *88*, 107–124. [CrossRef]
9. Ilgen, A.G.; Heath, J.E.; Akkutlu, I.Y.; Bryndzia, L.T.; Cole, D.R.; Kharaka, Y.K.; Kneafsey, T.J.; Milliken, K.L.; Pyrak-Nolte, L.J.; Suarez-Rivera, R.; et al. Shales at all scales: Exploring coupled processes in mudrocks. *Earth-Sci. Rev.* **2017**, *166*, 132–152. [CrossRef]
10. Neuzil, C.E. Permeability of clays and shales. *Annu. Rev. Earth Planet. Sci.* **2019**, *47*, 247–273. [CrossRef]
11. Masihi, M.; Shams, R.; King, P.R. Pore level characterization of Micro-CT images using percolation theory. *J. Petrol. Sci. Eng.* **2022**, *211*, 110113. [CrossRef]
12. Zang, J.; Liu, J.; He, J.; Zhang, X. Characterization of the pore structure in Chinese anthracite coal using FIB-SEM tomography and deep learning-based segmentation. *Energy* **2023**, *282*, 128686. [CrossRef]
13. Yao, J.; Liu, L.; Yang, Y.; Sun, H.; Zhang, L. Characterizing multi-scale shale pore structure based on multi-experimental imaging and machine learning. *Nat. Gas Ind. B* **2023**, *10*, 361–371. [CrossRef]
14. Li, S.; Dong, M.; Luo, P. A crossflow model for an interacting capillary bundle: Development and application for waterflooding in tight oil reservoirs. *Chem. Eng. J.* **2017**, *164*, 133–147. [CrossRef]
15. Yasuhara, H.; Elsworth, D.; Polak, A. A mechanistic model for compaction of granular aggregates moderated by pressure solution. *J. Geophys. Res. Solid Earth* **2003**, *108*, 2530. [CrossRef]
16. Čapek, P.; Hejtmánek, V.; Brabec, L.; Zikánová, A.; Kočiřík, M. Stochastic reconstruction of particulate media using simulated annealing: Improving pore connectivity. *Transp. Porous Med.* **2009**, *76*, 179–198.
17. Chen, D.; Liu, Y.; Wang, X.; Wang, M. Reconstruction of the microstructure based on hierarchical simulated annealing with erosion method. *Physica A* **2022**, *604*, 127694. [CrossRef]
18. Øren, P.E.; Bakke, S. Process based reconstruction of sandstones and prediction of transport properties. *Transp. Porous Med.* **2002**, *46*, 311–343.
19. Yao, S.; Wang, X.; Yuan, Q.; Zeng, F. Estimation of Shale Intrinsic Permeability with Process-Based Pore Network Modeling Approach. *Transp. Porous Med.* **2018**, *125*, 127–148. [CrossRef]
20. Hajizadeh, A.; Safekordi, A.; Farhadpour, F.A. A multiple-point statistics algorithm for 3D pore space reconstruction from 2D images. *Adv. Water Resour.* **2011**, *34*, 1256–1267. [CrossRef]
21. Wu, Y.; Lin, C.; Ren, L.; Yan, W.; An, S.; Chen, B.; Wang, Y.; Zhang, X.; You, C.; Zhang, Y. Reconstruction of 3D porous media using multiple-point statistics based on a 3D training image. *J. Nat. Gas Sci. Eng.* **2018**, *51*, 129–140. [CrossRef]
22. Yan, T.; Xu, X.; Liu, J.; Zhang, Y.; Arif, M.; Xu, X.; Wang, Q. Data-driven predictive model of coal permeability based on microscopic fracture structure characterization. *J. Rock Mech. Geotech.* **2025**, *17*, 4476–4489. [CrossRef]
23. Xi, Z.; Tang, S.; Zhang, S.; Qi, Y.; Wang, X. Evaluation of mechanical properties of porous media materials based on deep learning: Insights from pore structure. *Fuel* **2024**, *371*, 131923. [CrossRef]
24. Zhang, M.; Chen, W.; Huang, X.; Yuan, Q.; Zhao, Y.P. Hyperelastic constitutive relations for porous materials with initial stress. *J. Mech. Phys. Solids* **2024**, *193*, 105886. [CrossRef]
25. Katz, A.J.; Thompson, A.H. Fractal sandstone pores: Implications for conductivity and pore formation. *Phys. Rev. Lett.* **1985**, *54*, 1325. [CrossRef]
26. Jin, Y.; Wang, C.; Liu, S.; Quan, W.; Liu, X. Systematic definition of complexity assembly in fractal porous media. *Fractals* **2020**, *28*, 2050079. [CrossRef]
27. Zhao, M.; Jin, Y.; Liu, X.; Zheng, J.; Liu, S. Characterizing the Complexity Assembly of Pore Structure in a Coal Matrix: Principle, Methodology, and Modeling Application. *J. Geophys. Res. Solid Earth* **2020**, *125*, e2020JB020110. [CrossRef]
28. Zheng, J.; Liu, X.; Jin, Y.; Dong, J.; Wang, Q. Effects of surface geometry on advection-diffusion process in rough fractures. *Chem. Eng. J.* **2021**, *414*, 128745. [CrossRef]
29. Jin, Y.; Zheng, J.; Dong, J.; Wang, Q.; Liu, Y.; Wang, B.; Song, H. Fractal topography and complexity assembly in multifractals. *Fractals* **2022**, *30*, 2250052. [CrossRef]
30. Li, H.; He, S.; Radwan, A.E.; Xie, J.; Qin, Q. Quantitative analysis of pore complexity in lacustrine organic-rich shale and comparison to marine shale: Insights from experimental tests and fractal theory. *Energy Fuels* **2024**, *38*, 16171–16188. [CrossRef]
31. Fu, X.; Qin, Y.; Zhang, W.; Wei, C.; Zhou, R. Fractal classification and natural classification of coal pore structure based on migration of coal bed methane. *Chin. Sci. Bull.* **2005**, *50*, 66–71. [CrossRef]
32. Han, W.; Zhou, G.; Gao, D.; Zhang, Z.; Wei, Z.; Wang, H.; Yang, H. Experimental analysis of the pore structure and fractal characteristics of different metamorphic coal based on mercury intrusion-nitrogen adsorption porosimetry. *Powder Technol.* **2020**, *362*, 386–398. [CrossRef]

33. Duan, R.; Xu, Z.; Dong, Y.; Liu, W. Characterization and classification of pore structures in deeply buried carbonate rocks based on mono-and multifractal methods. *J. Petrol. Sci. Eng.* **2021**, *203*, 108606. [CrossRef]
34. Yao, Y.; Liu, D.; Tang, D.; Tang, S.; Huang, W.; Liu, Z.; Che, Y. Fractal characterization of seepage-pores of coals from China: An investigation on permeability of coals. *Comput. Geosci.* **2009**, *35*, 1159–1166. [CrossRef]
35. Lai, J.; Wang, G.; Wang, Z.; Chen, J.; Pang, X.; Wang, S.; Zhou, Z.; He, Z.; Qin, Z.; Fan, X. A review on pore structure characterization in tight sandstones. *Earth-Sci. Rev.* **2018**, *177*, 436–457. [CrossRef]
36. Jin, Y.; Zhao, B.; Yang, Y.; Dong, J.; Song, H.; Tian, Y.; Pan, J. Intelligent Extraction of Complexity Types in Fractal Reservoir and its Significance to Estimate Transport Property. *Fractals* **2024**, *32*, 2450070. [CrossRef]
37. Zheng, J.; Jin, Y.; Dong, J.; Liu, S.; Zhang, Q.; Song, H.; Huang, P. Reexamination of the permeability-aperture relationship for rough fractures with mismatched self-affine surfaces. *J. Hydrol.* **2022**, *609*, 127727. [CrossRef]
38. Liu, Z.; Han, J.; Yang, H.; Lv, J.; Dong, S. A new model for coal gas seepage based on fracture-pore fractal structure characteristics. *Int. J. Rock Mech. Min.* **2024**, *173*, 105626. [CrossRef]
39. Perrier, E.; Bird, N.; Rieu, M. Generalizing the fractal model of soil structure: The pore–solid fractal approach. *Geoderma* **1999**, *88*, 137–164. [CrossRef]
40. Pia, G.; Sanna, U. Intermingled fractal units model and electrical equivalence fractal approach for prediction of thermal conductivity of porous materials. *Appl. Therm. Eng.* **2013**, *61*, 186-192. [CrossRef]
41. Cheng, H.; Wang, F.; Yang, G.; Guan, X.; Cheng, Z.; Li, H.; Yu, C.; Feng, G.; Yuan, Y. Prediction of relative permeability from capillary pressure based on the fractal capillary bundle model. *Appl. Therm. Eng.* **2024**, *239*, 122093. [CrossRef]
42. Jin, Y.; Li, X.; Zhao, M.; Liu, X.; Li, H. A mathematical model of fluid flow in tight porous media based on fractal assumptions. *Int. J. Heat Mass Transf.* **2017**, *108*, 1078–1088. [CrossRef]
43. Jin, Y.; Liu, D.; Zheng, J.; Dong, J.; Wang, Q.; Huang, H.; Zhao J.; Liu S.; Song H. Principle and approach for the characterization of complexity types and their assembly pattern in natural fractal porous reservoir. *Chin. J. Rock Mech. Eng.* **2023**, *42*, 781–797. (In Chinese)
44. Friesen, W.I.; Mikula, R.J. Fractal dimensions of coal particles. *J. Colloid Interface Sci.* **1987**, *120*, 263–271. [CrossRef]
45. Pfeifer, P.; Wu, Y.J.; Cole, M.W.; Krim, J. Multilayer adsorption on a fractally rough surface. *Phys. Rev. Lett.* **1989**, *62*, 1997–2000. [CrossRef]
46. Xie, W.; Wang, M.; Wang, H.; Duan, H. Multi-scale fractal characteristics of pores in transitional shale gas reservoir. *Nat. Gas Geosci.* **2022**, *33*, 451–460. (In Chinese)
47. Li, A.; Ding, W.; Jiu, K.; Wang, Z.; Wang, R.; He, J. Investigation of the pore structures and fractal characteristics of marine shale reservoirs using NMR experiments and image analyses: A case study of the Lower Cambrian Niutitang Formation in northern Guizhou Province, South China. *Mar. Petrol. Geol.* **2018**, *89*, 530–540. [CrossRef]
48. Mishra, S.; Mendhe, V.A.; Varma, A.K.; Kamble, A.D.; Sharma, S.; Bannerjee, M.; Kalpana, M.S. Influence of organic and inorganic content on fractal dimensions of Barakar and Barren Measures shale gas reservoirs of Raniganj basin, India. *J. Nat. Gas Sci. Eng.* **2018**, *49*, 393–409. [CrossRef]
49. Liu, S.; Xue, H.; Zhao, M. Pore Structure and Fractal Characteristics of Coal Measure Shale in the Wuxiang Block in the Qinshui Basin. *Processes* **2023**, *11*, 3362. [CrossRef]
50. Yang, F.; Ning, Z.; Liu, H. Fractal characteristics of shales from a shale gas reservoir in the Sichuan Basin, China. *Fuel* **2014**, *115*, 378–384. [CrossRef]
51. Zhao, C.; Bao, Z.; Li, Z.; Qi, Y.; Chen, L.; Wang, H.; Zhang, Y.; Fang, F. Characterization and fractal characteristics of nano-scale pore structure in shale gas reservoirs: A case study of the deep Longmaxi Formation, Zigong region, Southern Sichuan Basin, China. *Front. Earth Sci.* **2024**, *12*, 1410437. [CrossRef]
52. Wang, R.; Feng, H.; Liu, C. Applicability of mercury intrusion method and nitrogen adsorption method in characterizing pore structure of high-rank coal. *Oil Drill. Prod. Technol.* **2024**, *46*, 112–118. (In Chinese)
53. Song, H.; An, H.; Liu, S.; Yu, Z.; Jin, Y.; Wang, B. Controlling geological factors and coalbed methane enrichment areas in southern Wuxiang block, Qinshui Basin. *J. China Coal Soc.* **2021**, *46*, 3974-3987. (In Chinese)
54. Shao, L.Y.; Yang, Z.Y.; Shang, X.X.; Xiao, Z.H.; Wang, S.; Zhang, W.L.; Zheng, M.Q.; Lu, J.; Lithofacies palaeogeography of the Carboniferous and Permian in the Qinshui basin, Shanxi Province, China. *J. Palaeogeogr.* **2015**, *4*, 384–412. [CrossRef]
55. *GB/T 21650.1-2008*; Pore Size Distribution and Porosity of Solid Materials by Mercury Porosimetry and Gas Adsorption-Part 1: Mercury Porosimetry. Standards Press of China: Beijing, China, 2008. (In Chinese)
56. *SY/T 6154-1995*; Petroleum and Natural Gas Industry-Steel Pipe for Pipeline Transportation Systems-Technical Delivery Conditions. Petroleum Industry Press: Beijing, China, 1995. (In Chinese)
57. Hu, B.; Cheng, Y.; Pan, Z. Classification methods of pore structures in coal: A review and new insight. *Gas Sci. Eng.* **2023**, *110*, 204876. [CrossRef]

58. Fu, H.; Tang, D.; Xu, T.; Xu, H.; Tao, S.; Li, S.; Yin, Z.; Chen, B.; Zhang, C.; Wang, L. Characteristics of pore structure and fractal dimension of low-rank coal: A case study of Lower Jurassic Xishanyao coal in the southern Junggar Basin, NW China. *Fuel* **2017**, *193*, 254–264. [CrossRef]
59. Li, Y.; Lu, G.; Rudolph, V. Compressibility and fractal dimension of fine coal particles in relation to pore structure characterisation using mercury porosimetry. *Part. Part. Syst. Charact.* **1999**, *16*, 25–31. [CrossRef]
60. Li, Z.; Liu, D.; Cai, Y.; Yao, Y.; Wang, H. Pore structure and compressibility of coal matrix with elevated temperatures by mercury intrusion porosimetry. *Energy Explor. Exploit.* **2015**, *33*, 809–826. [CrossRef]
61. Li, W.; Liu, H.; Song, X. Multifractal analysis of Hg pore size distributions of tectonically deformed coals. *Int. J. Coal Geol.* **2015**, *144*, 138–152. [CrossRef]
62. Toda, Y.; Toyoda, S. Application of mercury porosimetry to coal. *Fuel* **1972**, *51*, 199–201. [CrossRef]
63. Lan, Y.; Moghanloo, R.G.; Davudov, D. Pore compressibility of shale formations. *SPE J.* **2017**, *22*, 1778–1789. [CrossRef]

Disclaimer/Publisher's Note: The statements, opinions and data contained in all publications are solely those of the individual author(s) and contributor(s) and not of MDPI and/or the editor(s). MDPI and/or the editor(s) disclaim responsibility for any injury to people or property resulting from any ideas, methods, instructions or products referred to in the content.